GSA DATA REPOSITORY 2012058

The origin of intracellular structures in Ediacaran metazoan embryos

James D. Schiffbauer[1,2]*, Shuhai Xiao[2], Kriti Sen Sharma[3], and Ge Wang[3]
[1]*Nanoscale Characterization and Fabrication Laboratory, Institute for Critical Technology and Applied Science, Virginia Polytechnic Institute and State University, Blacksburg, Virginia 24061, USA*
[2]*Department of Geosciences, Virginia Polytechnic Institute and State University, Blacksburg, Virginia 24061, USA*
[3]*School of Biomedical Engineering & Sciences, Virginia Polytechnic Institute and State University, Blacksburg, Virginia 24061, USA*
*Corresponding author email: jdschiff@vt.edu

EXPANDED METHODS

Fossil Extraction

Fossils were extracted from light grey Doushantuo dolomitic phosphorite (Dornbos et al., 2006) using standard acetic acid maceration techniques (Xiao and Knoll, 2000), in which ~100 gram rock fragments were submersed in 10% acetic acid for approximately 24–48 hours, until dolomitic matrix was dissolved and phosphatic microfossils were freed. The microfossils were hand-picked from maceration residue and examined under reflected light microscopy.

Microcomputed X-Ray Tomography (microCT)

Six multi-celled blastula-like fossils (*Parapandorina raphospissa*) were identified for microCT analysis. They were mounted to Omniprobe® tungsten needles using Loctite® ultragel superglue. Prior to mounting, the tungsten needles were trimmed to a length of 15 mm, and the cut edges were polished using 400-grit silicon carbide lapidary papers to remove sharp edges and uneven surfaces. After being mounted, the fossils were examined in a microCT scanner (Xradia MicroXCT-400) at a beam voltage of 80 kV and energy of 8 W, using a 20× objective, 180° scan rotation, and 271 frames at a collection time of 450 seconds per frame (run time ~35 hours). One 16-celled specimen showed numerous intracellular structures. This specimen was prepared for further analyses and the results are reported in this paper.

Fracturing and Polishing

After the initial microCT scanning, the needle-mounted specimen with intracellular structures was affixed to a standard scanning electron microscopy (SEM) aluminum stub using high-conductivity copper tape and broken using a vacuum needle along an existing fracture that was visible in the initial microCT analysis. This fractured specimen, with approximately half of the specimen remaining attached to the tungsten needle, was removed from the aluminum SEM stub and rescanned with the microCT system in order to verify the portion of the remaining specimen. The rescan was carried out with a beam voltage of 50 kV and energy of 5 W, using a 20× objective, 180° scan rotation, and 750 frames at a collection time of 2 seconds per frame

(run time ~2.5 hours). Following the rescan, the fractured specimen was reattached to a SEM stub and sputter coated with 2.5 nm of Au-Pd using a Cressington 208HR high-resolution sputter-coater. Initial backscattered electron z-contrast and secondary electron analyses were conducted on the fractured surface of the specimen following the procedures outlined below. After these initial analyses, the fractured specimen was placed in a 25.4 mm-diameter Teflon mold, with the fractured surface facing up, and embedded in low viscosity 2-part epoxy. The embedded specimen was then placed in a vacuum oven at 60°C for 12 hours to remove bubbles and facilitate curing. The hardened epoxy puck was removed from the Teflon mold, and the top surface was trimmed with a Dremel tool to within 5 mm of the fractured surface. The last ~5 mm of epoxy was removed via lapidary polishing (at 200-grit and then 800-grit silicon carbide) to expose the fractured face. All subsequent polishing used 1200-grit silicon carbide lapidary paper, with repeated examination under reflected light microscopy which allowed for the identification and location of intracellular structures. Final polish was conducted with 0.3 μm alumina (aluminum oxide) on a microfiber cloth to ensure a smooth surface for further analysis, and to avoid potential carbon contamination from carbide-based polishing compounds. Following final polishing, a 2.5 nm Au-Pd coat was applied to prepare the polished surface for SEM analysis. After SEM analysis, the specimen was subsequently repolished and additional SEM analysis was repeated, at regular intervals of approximately 25–30 μm through the specimen.

Scanning Electron Microscopy of Fractured and Polished Surfaces

SEM analysis was conducted on a FEI Company Quanta 600 field emission environmental scanning electron microscope under high vacuum mode. The fractured surface was analyzed in both backscattered electron z-contrast (BSE-Z) mode using a quad-channel solid-state backscatter detector and secondary electron (SE) mode using an Everhart-Thornley detector (ETD). Polished surfaces were analyzed in SE, BSE-Z, and backscattered electron topography (BSE-T) modes. In standard SE detection using an ETD, surfaces with topographic relief produce differences in electron escape distance and therefore regions with differing emission of secondary electrons (low-energy sample electrons emitted from specimen-atom k-orbitals by inelastic scattering interactions with beam electrons). The variation in brightness observed in an SE image directly corresponds to the number of secondary electrons reaching the detector, resulting in a well-defined three-dimensional representation of the surface (Goldstein et al., 1981). BSE-T detection, on the other hand, maximizes the solid angle of detection as the detector is concentrically positioned with the beam rather than at an angle like ETDs. When all four sectors of the detector are used in unison to symmetrically collect backscattered electrons (high-energy beam electrons backscattered or reflected from the sample interaction volume by elastic scattering interactions with specimen atoms) about the beam, an atomic-number or z-contrast image is produced because heavier elements more strongly backscatter electrons and therefore appear brighter than light elements. When only one side (two sectors) of the detector are used asymmetrically, or directionally, to collect backscattered electrons, the resulting contrast shows specimen topography from the active detector side (Goldstein et al., 1981). Numerous BSE-Z and BSE-T images, each 128 μm wide, of the polished surface were compiled into image montages to assure high-resolution capabilities across the entire surface. Regions of interest, including cell boundaries, NIS structures, and cell lumen, were then analyzed semi-quantitatively (using both point analyses [45,000 ms live collection time, variable real time] and elemental mapping [600,000 ms live collection time, variable real time]) and quantitatively (100 μm^2 region scans, 300,000 ms live collection time, variable real time) with an integrated Bruker AXS

Quantax 400 energy dispersive x-ray spectrometer (EDS) with a high-speed silicon drift detector (SDD). All other operating conditions were held constant: detector take off angle = 35°, working distance = 10.0 mm, accelerating voltage = 20 keV, and beam current/probe diameter = 5.0 spot size. Atomic weight normalization as well as both Au-Pd coating and ZAF correction factors were applied to semi-quantitative point spectra.

Atomic Force Microscopy and Electron Probe Microanalysis

After observing hints of topographical relief in BSE-T montages, the polished specimen was examined using atomic force microscopy (AFM) to quantify the topographic relief, and to resolve its potential effect on BSE imaging. The sample was analyzed using a Veeco Dimension 3100 Nanoman AFM under contact mode, with scan regions ranging from 2500 μm^2 to 10000 μm^2. Finally, a Cameca SX-50 electron probe microanalyzer (EPMA) was utilized (in WDS mapping mode with an integrated Bruker SDD system, at 15 keV beam voltage and a 24-mm working distance) to determine the distribution of trace elements.

REFERENCES CITED

Dornbos, S. Q., Bottjer, D. J., Chen, J. Y., Gao, F., Oliveri, P., and Li, C. W., 2006, Environmental controls on the taphonomy of phosphatized animals and animal embryos from the Neoproterozoic Doushantuo Formation, southwest China: Palaios, v. 21, p. 3-14.

Goldstein, G. I., Newbury, D. E., Echlin, P., Joy, D. C., Fiori, C., and Lifshin, E., 1981, Scanning electron microscopy and x-ray microanalysis, New York, Plenum Press.

Xiao, S., and Knoll, A. H., 2000, Phosphatized animal embryos from the Neoproterozoic Doushantuo Formation at Weng'an, Guizhou, South China: Journal of Paleontology, v. 74, no. 5, p. 767-788.

DATA REPOSITORY MOVIES, FIGURES, AND TABLES

Movie DR1: Top-down microCT slice-and-view of the full specimen.

Movie DR2: Top-down microCT slice-and-view of the fractured specimen.

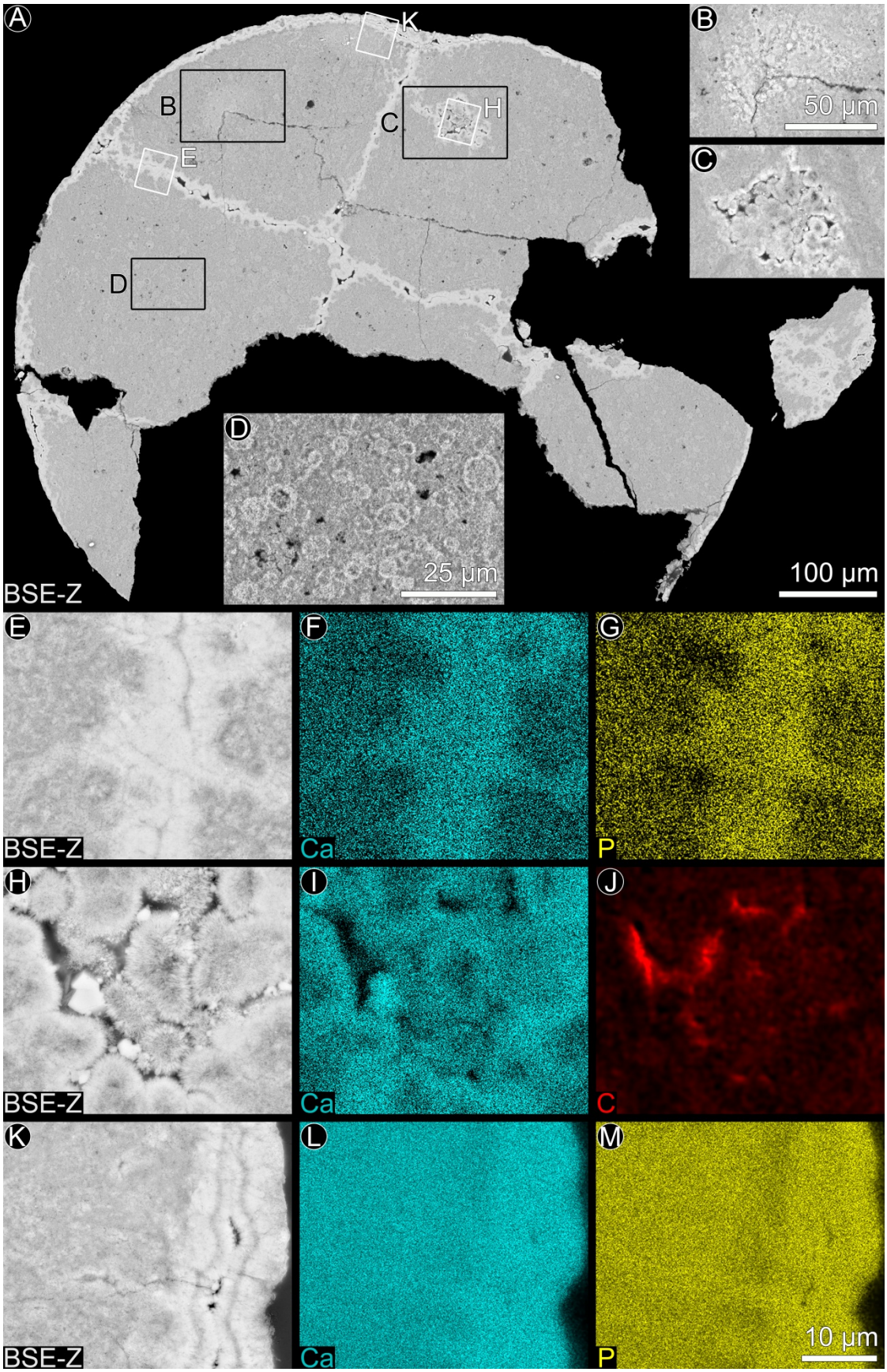
A
K
B
C
H
E
D
B
50 µm
C
D
25 µm
BSE-Z
100 µm
E
F
G
BSE-Z
Ca
P
H
I
J
BSE-Z
Ca
C
K
L
M
BSE-Z
Ca
P
10 µm

Figure DR1 (previous page): BSE-Z montage and EDS elemental maps of a polished surface approximately 25–30 µm prior to polished surface shown in Fig. 2. (A) BSE-Z image montage with labeled boxes corresponding to (B–M). (B and C) Magnified views of NIS from a different polished surface but positionally corresponding to labeled boxes in (A). (D) Magnified view of LIS. (E–G) BSE-Z, Ca map, and P map of a cell boundary region. (H–J) BSE-Z, Ca map, and C map of a NIS region. (K–M) BSE-Z, Ca map, and P map of outer cell boundary (right) and cell lumen (left) regions. Centripetally growing botryoids indicate void-filling cementation in space between cell and outer envelope. Scale in (M) applies to (E–M).

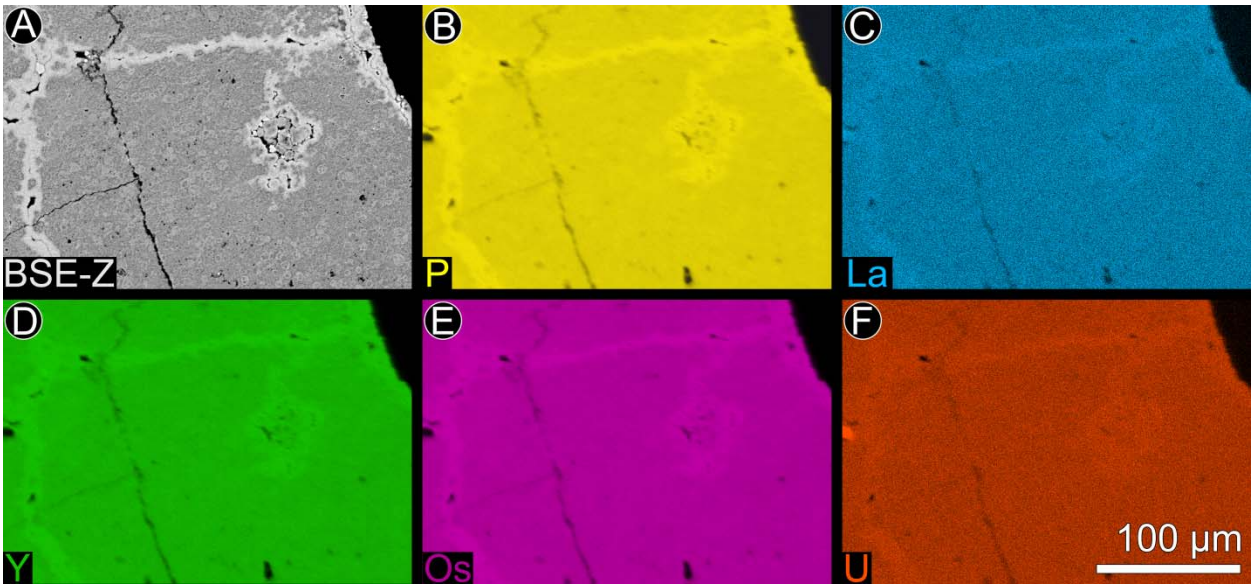

Figure DR2: EPMA WDS elemental maps of cell lumen, NIS and cell boundary. (A) BSE-Z image of mapped region (approximately equivalent to the upper right quadrant of Fig. DR1A). (B) Baseline map illustrating higher perceived elemental abundance of P due to higher packing density of apatite crystals. (C–F) Corresponding maps, respectively, of REEs (La and Y), transition metal (Os), and actinide metal (U) concentrations showing identical relative abundance trends.

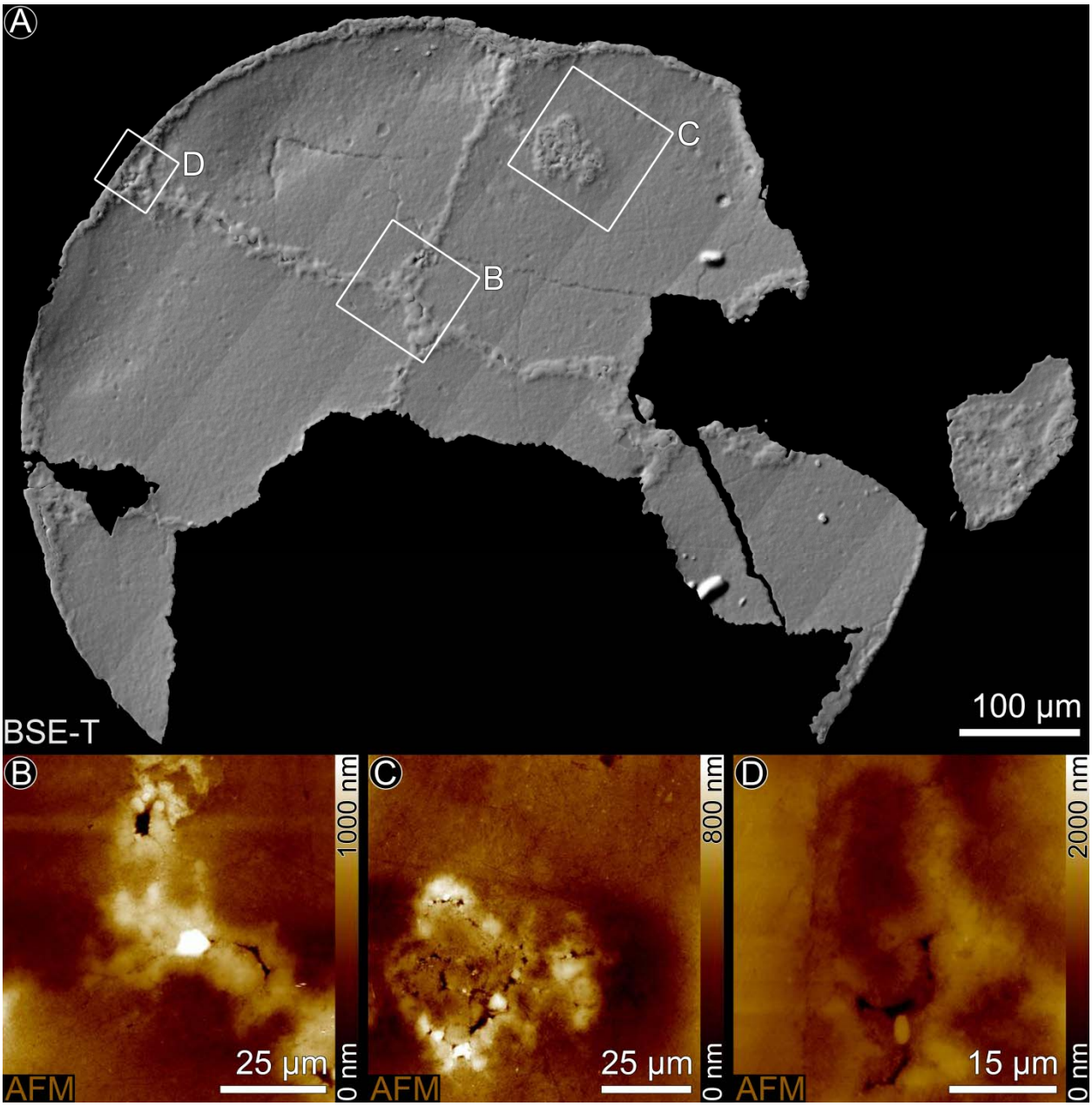

Figure DR3: BSE-T montage and AFM topography of a polished surface. (A) BSE-T image montage with labeled boxes corresponding to AFM topographic maps. (B–D) AFM topographic maps of a cell boundary region (maximum relief = ~500.5 nm), a NIS structure region (maximum relief = ~360.9 nm), and an outer cell boundary region (maximum relief = ~287.9 nm). Topographic scale labeled at right for each frame.

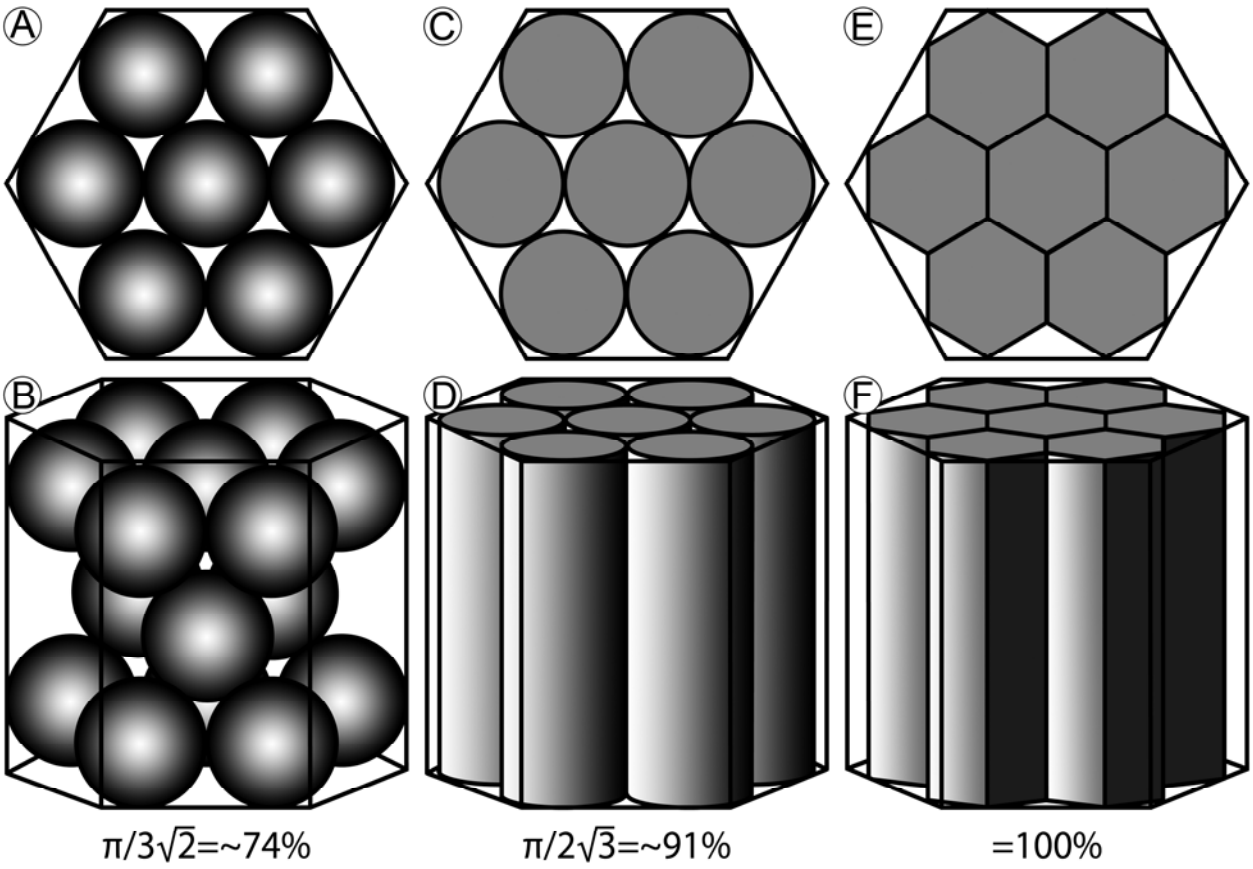

Figure DR4: Three-dimensional representations of hexagonal close packing (hcp) for different crystal texture approximations as viewed from top (upper) and side (lower). (A and B) Sphere hcp model representing equant apatite crystals of cell lumen. (C and D) Rounded cylinder hcp model representing aligned prismatic apatite botryoids in cell boundaries, NIS, and LIS rims. (E and F) Hexagonal prism hcp model showing seamless tessellation, a model perhaps better representing aligned prismatic apatite crystals in cell boundary, NIS, and LIS botryoids.

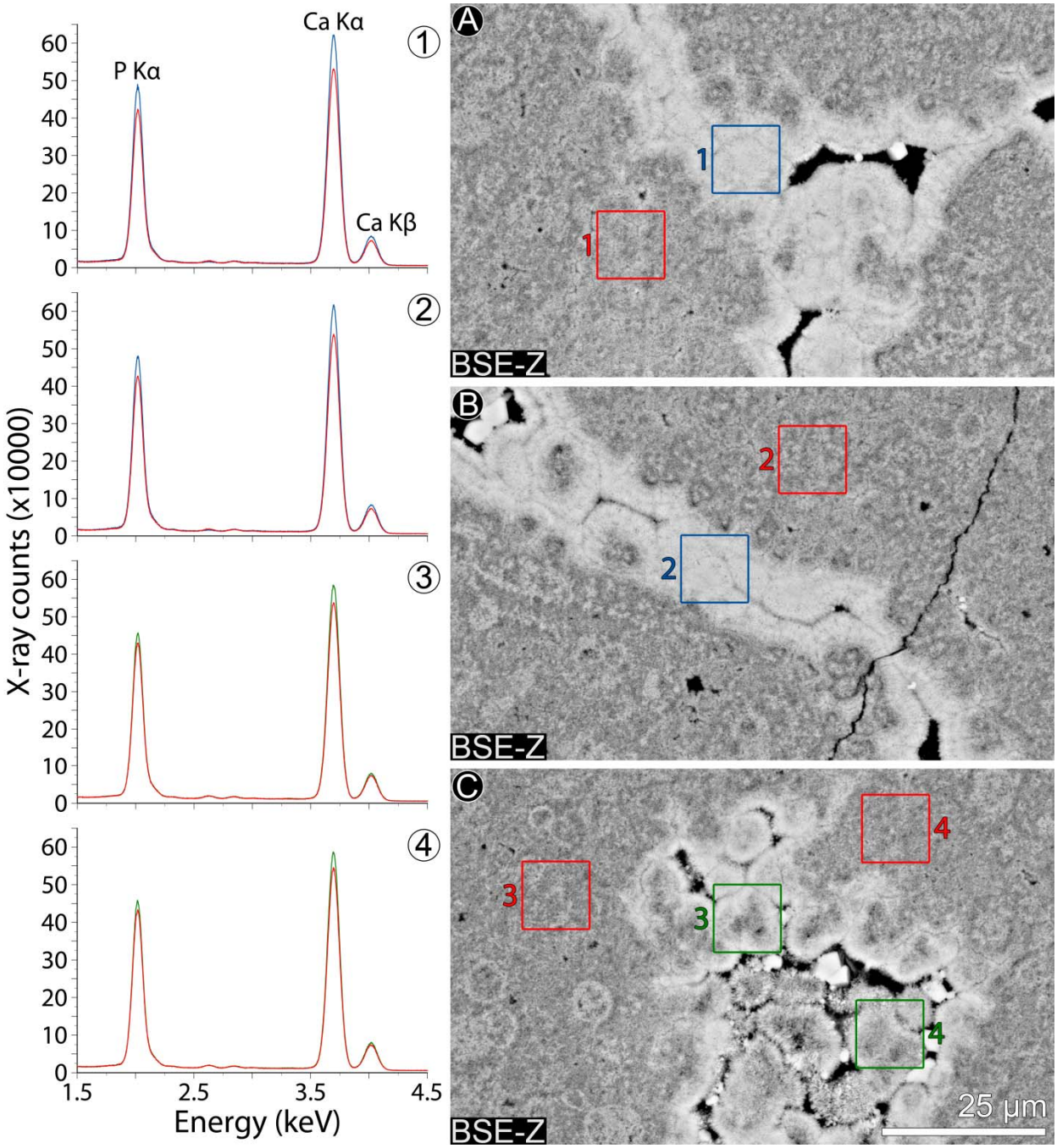

Figure DR5: Quantitative EDS spectra with corresponding 100 µm^2 analyzed regions. (A–C) BSE-Z images of cell boundaries (blue boxes and lines on spectral graphs 1 and 2), cell lumen (red boxes and lines on spectral graphs 1–4), and NIS (green boxes and lines on spectral graphs 3–4). All box numbers correspond to graph numbers. Analyzed regions were specifically chosen to avoid obvious void spaces. Elemental bands analyzed for peak heights include only the Kα for P and Ca, although the Ca Kβ band is also labeled here.

Table DR1: Full EDS point data reported in normalized weight percentage.

Category C	C	O	F	P	Ca	Ca:P
Lumen	4.1	27.8	7.1	18.6	42.5	2.3
Lumen	3.0	29.6	10.5	17.8	39.1	2.2
Lumen	4.0	28.6	8.5	18.2	40.7	2.2
Lumen	4.2	28.4	8.7	18.2	40.5	2.2
Lumen	4.3	28.7	8.3	18.3	40.5	2.2
Lumen	4.8	28.1	11.7	17.5	37.9	2.2
Lumen	5.4	27.6	7.4	18.2	41.4	2.3
Lumen	5.4	27.5	8.0	18.2	40.9	2.2
Lumen	3.4	29.0	11.3	17.6	38.6	2.2
Lumen	4.3	29.1	8.5	17.7	40.4	2.3
Lumen	4.0	29.3	10.3	17.5	39.0	2.2
Lumen	4.2	28.0	9.4	18.3	40.1	2.2
Lumen	3.9	29.8	13.0	16.9	36.4	2.2
Lumen	4.3	28.0	6.7	18.6	42.5	2.3
Lumen	3.6	29.4	9.5	17.9	39.6	2.2
Lumen	3.9	29.1	11.2	17.5	38.2	2.2
Lumen	4.0	29.9	10.6	17.3	38.3	2.2
Lumen	4.5	30.1	12.2	16.8	36.5	2.2
Lumen	3.8	30.0	11.2	17.2	37.7	2.2
Lumen	4.4	29.2	8.9	17.8	39.8	2.2
Lumen	3.9	28.6	10.7	17.7	39.1	2.2
Lumen	4.6	29.8	11.7	16.9	37.0	2.2
Lumen	3.2	29.8	10.7	17.6	38.7	2.2
Lumen	3.8	30.4	11.6	17.1	37.1	2.2
Lumen	4.1	29.3	9.2	17.8	39.6	2.2
Lumen	4.7	28.7	10.5	17.4	38.7	2.2
Lumen	4.4	29.0	10.6	17.4	38.6	2.2
Lumen	4.7	27.4	9.7	18.1	40.0	2.2
Lumen	4.8	29.0	11.2	17.3	37.7	2.2
Lumen	4.0	28.8	10.9	17.7	38.6	2.2
Mean ± 1σ	4.2 ± 0.5	28.9 ± 0.8	10.0 ± 1.6	17.7 ± 0.5	39.2 ± 1.6	2.2 ± 0.1
NIS	0.8	29.8	11.0	18.5	40.0	2.2
NIS	0.7	29.9	11.1	18.4	40.0	2.2
NIS	1.0	29.9	12.6	18.0	38.6	2.1
NIS	2.3	30.3	10.4	18.0	39.1	2.2
NIS	2.1	28.7	11.7	18.3	39.3	2.1
NIS	1.2	28.3	11.0	18.5	41.0	2.2
NIS	4.1	28.6	8.8	18.0	40.5	2.3
NIS	1.7	28.9	11.2	18.3	39.9	2.2
NIS	4.3	29.5	10.7	17.4	38.1	2.2
NIS	4.5	28.5	7.8	18.3	40.9	2.2
NIS	3.6	28.7	9.2	18.1	40.3	2.2
NIS	4.3	29.6	9.9	17.2	39.0	2.3
NIS	5.7	27.8	6.2	18.3	42.0	2.3
NIS	4.4	28.0	9.5	17.9	40.2	2.3
NIS	5.0	29.2	8.3	17.8	39.7	2.2
NIS	10.3	29.8	9.8	15.5	34.5	2.2
NIS	6.4	27.8	8.0	17.5	40.3	2.3

NIS	4.6	31.1	13.2	16.1	35.0	2.2
NIS	3.0	29.2	11.5	17.9	38.4	2.2
NIS	9.7	25.4	5.1	17.9	42.0	2.3
NIS	4.7	27.8	9.0	18.1	40.4	2.2
NIS	4.1	27.7	9.7	18.2	40.3	2.2
NIS	3.1	28.9	10.2	18.3	39.6	2.2
NIS	3.0	29.0	11.5	17.9	38.5	2.1
NIS	3.6	29.6	11.6	17.4	37.7	2.2
NIS	4.8	30.1	10.5	17.0	37.6	2.2
NIS	5.8	28.9	9.7	17.4	38.2	2.2
NIS	3.9	29.3	12.4	17.2	37.2	2.2
NIS	4.1	29.8	12.1	16.9	37.0	2.2
NIS	4.2	28.7	10.4	17.6	39.0	2.2
Mean ± 1σ	4.0 ± 2.2	29.0 ± 1.1	10.1 ± 1.8	17.7 ± 0.7	39.1 ± 1.7	2.2 ± 0.1
Boundary	2.2	28.6	8.1	18.9	42.3	2.2
Boundary	5.1	29.9	8.8	17.1	39.2	2.3
Boundary	2.0	27.8	8.8	19.2	42.3	2.2
Boundary	3.9	29.3	11.3	17.3	38.2	2.2
Boundary	1.4	28.2	6.8	19.3	44.3	2.3
Boundary	4.4	29.4	9.7	17.4	39.2	2.3
Boundary	5.4	28.4	8.3	18.0	39.9	2.2
Boundary	2.4	30.1	10.7	17.9	38.9	2.2
Boundary	5.5	28.3	9.0	17.8	39.4	2.2
Boundary	4.0	29.2	12.7	17.0	37.1	2.2
Boundary	4.5	29.0	11.2	17.4	37.9	2.2
Boundary	4.3	30.2	10.9	17.1	37.4	2.2
Boundary	2.7	30.3	13.8	17.0	36.2	2.1
Boundary	3.2	30.3	12.2	17.2	37.1	2.2
Boundary	1.5	29.4	10.1	18.2	40.8	2.2
Boundary	3.1	28.1	10.7	18.6	39.5	2.1
Boundary	1.8	28.7	8.8	18.5	42.2	2.3
Boundary	1.8	29.4	10.1	18.4	40.3	2.2
Boundary	1.9	26.5	8.4	19.4	43.9	2.3
Boundary	1.7	29.4	9.6	18.8	40.6	2.2
Boundary	3.3	29.5	10.7	17.7	38.9	2.2
Boundary	4.3	28.4	8.1	18.2	41.1	2.3
Boundary	2.3	28.4	8.1	19.1	42.0	2.2
Boundary	4.0	29.7	12.1	17.2	37.1	2.2
Boundary	4.3	29.3	11.6	17.1	37.7	2.2
Boundary	5.0	29.8	10.9	17.0	37.4	2.2
Boundary	3.7	30.8	13.4	16.6	35.4	2.1
Boundary	5.8	29.1	9.4	17.2	38.5	2.2
Boundary	4.9	30.2	11.7	16.4	36.8	2.2
Boundary	4.9	29.2	9.8	17.6	38.5	2.2
Mean ± 1σ	3.5 ± 1.3	29.2 ± 0.9	10.2 ± 1.7	17.8 ± 0.8	39.3 ± 2.3	2.2 ± 0.1
Full mean ± 1σ	3.9 ± 1.5	29.0 ± 0.9	10.1 ± 1.7	17.7 ± 0.7	39.2 ± 1.9	2.2 ± 0.1